Chapter 3

Reconstruction of $B^+ \to \rho^+\rho^0$

The $B^+ \to \rho^+\rho^0$ candidate selection is based on the skimmed HadronB events. In the following, before discussing the B reconstruction, we briefly describe the HadronB selection, and the measurement of the number of $B\bar{B}$ events.

3.1 HadronB Events Selection

The KEKB operates at the $\Upsilon(4S)$ resonance. Besides the signal B production $e^+e^- \to \Upsilon(4S) \to B\bar{B}$, there are also other processes with comparable or substantially larger cross sections. In the following, we list the major processes.

- $e^+e^- \to q\bar{q}$, where $(q = u,\ d,\ s,\ c)$
- τ-pair, $e^+e^- \to \tau^+\tau^-$
- μ-pair, $e^+e^- \to \mu^+\mu^-$
- Bhabha, $e^+e^- \to e^+e^-$
- two photon processes, $e^+e^- \to e^+e^-\gamma\gamma \to e^+e^-q\bar{q}$

The latter four processes are collectively called as the non-hadronic background. In general, the non-hadronic events have a lower multiplicity compared to the B decays. Each track carries a relatively large cms energy. Both the continuum $q\bar{q}$ background and the non-hadronic background tend to be collimated along a single axis. In order to reduce the non-hadronic background as well as beam gas events and $q\bar{q}$ continuum background, a hadronic selection criteria [36] based on the reconstructed tracks and ECL cluster is applied. We define good tracks as tracks with a transverse momentum $p_t > 100$ MeV/c, and originate from within $|\Delta r| < 2$ cm and $|\Delta z| < 4$ cm of the nominal interaction point; good clusters are clusters in the ECL with an energy greater than 100 MeV; good photons are good clusters in the polar region of $17° < \theta < 150°$ that cannot be associated with tracks in the CDC.

- The number of good tracks in an event is required to be at least 3.
- The sum of good track momenta and good photon energies in an event is required to be greater than $0.2\sqrt{s}$, where s is the square of the cms energy, $\sqrt{s} = 10.58$ GeV.
- The sum of the z components of momenta of each good track and good photon is required to be balanced around zero, $|p_z| < 0.5\sqrt{s}$.
- The sum of good cluster energies in the ECL of region $17° < \theta < 150°$ is required to satisfy $0.1\sqrt{s} < E_{sum} < 0.8\sqrt{s}$. The lower threshold removes the low energy backgrounds, while the upper one removes Bhabha events.
- The number of clusters in the ECL within the fiducial volume of $-0.7 < \cos\theta < 0.9$ is required to be greater than one, since for Bhabha events, most clusters have a very shallow dip angle.
- The larger invariant mass (HJM) of particles in the two hemisphere, which is split by a plane perpendicular to the thrust axis, is greater than 1.8 GeV. For τ-pair events, HJM is essentially the τ invariant mass (1.777 GeV).
- The average cluster energy, defined as E_{total}/n, where E_{total} is the sum of good cluster energies in the ECL, n is the number of clusters. For Bhabha events, the electrons make clusters in the ECL that have a large energy. The cut can further remove Bhabha background.

The cut efficiency and the final cross section for each background are listed in Table 3.1. As we can see, little non-hadronic events can pass through the hadronic selection, while the $q\bar{q}$ continuum background becomes dominant. The events passed through the hadronic selection are called "HadronB" events.

process	$B\bar{B}$	$q\bar{q}$	$\tau^+\tau^-$	Bhabha	$\gamma\gamma$
ϵ	0.991	0.795	0.049	0.00002	0.0004
σ (nb)	1.09	2.62	0.05	0.001	0.004

Table 3.1: The efficiencies and cross sections for various processes applied the hadronic selection.

3.2 The Number of $B\bar{B}$

To calculate the branching fraction for the $B^{\pm} \to \rho^{\pm}\rho^0$ decay, the number of $B^{\pm}$ mesons is needed. As mentioned, neutral B meson and charged B meson are almost equally

produced from $\Upsilon(4S)$. Here we assume equal production rates for $B^0\bar{B}^0$ and B^+B^-, following the prescription of the Particle Data Group [37]. So the number of B (B^+ and B^-) mesons is equal to the sum of the numbers of $B^0\bar{B}^0$ pairs and B^+B^- pairs. In the HadronB events, since the major components are the $B\bar{B}$ and $q\bar{q}$ events, the number of events on $\Upsilon(4S)$ resonance is given by,

$$N^{on} = N_{B\bar{B}} + N^{on}_{q\bar{q}}.$$

The number of $q\bar{q}$ continuum events is given by

$$N_{q\bar{q}} = \sigma_{q\bar{q}}\mathcal{L} = \frac{\sigma^0_{q\bar{q}}}{s}\mathcal{L}, \tag{3.1}$$

where s is the square of the cms energy, $\sigma_{q\bar{q}}$ is the cross section for $q\bar{q}$ production, which is proportional to $1/s$. Here we define $\sigma^0_{q\bar{q}}$, which is not s dependent any more.

The contribution of $q\bar{q}$ on resonance is estimated from data sample taken below the $\Upsilon(4S)$ threshold, called off-resonance data. From Equation 3.1, the number of $q\bar{q}$ events of off-resonance is given by

$$N^{off}_{q\bar{q}} = \frac{\sigma^0_{q\bar{q}}}{s^{off}}\mathcal{L}^{off}. \tag{3.2}$$

The number of $q\bar{q}$ events on resonance is given by

$$N^{on}_{q\bar{q}} = \frac{\sigma^0_{q\bar{q}}}{s^{on}}\mathcal{L}^{on}. \tag{3.3}$$

By substituting Equation 3.2 into Equation 3.3, we obtain,

$$\frac{N^{on}_{q\bar{q}}}{N^{off}_{q\bar{q}}} = \frac{s^{off}\mathcal{L}^{on}}{s^{on}\mathcal{L}^{off}}. \tag{3.4}$$

The Equation 3.4 is deduced for $q\bar{q}$ events, it is also true for the continuum production of any fermion pair. We define the ratio α,

$$\alpha = \frac{N^{on}_{q\bar{q}}}{N^{off}_{q\bar{q}}} = \frac{N^{on}_{e^+e^-}}{N^{off}_{e^+e^-}} = \frac{N^{on}_{\mu^+\mu^-}}{N^{off}_{\mu^+\mu^-}} = \frac{s^{off}\mathcal{L}^{on}}{s^{on}\mathcal{L}^{off}},$$

where $N_{e^+e^-}$ is the number of $e^+e^- \to e^+e^-$ Bhabha events, $N_{\mu^+\mu^-}$ is the number of $e^+e^- \to \mu^+\mu^-$ μ-pair events. Therefore, there are two independent ways to determine α. We use the average of the two values measured by the two methods to estimate the number of $q\bar{q}$ events,

$$\alpha = 0.5(\alpha_{ee} + \alpha_{\mu\mu}).$$

Finally, we determine the number of $B\bar{B}$ by [38]

$$N_{BB} = N^{on} - \alpha N^{off}_{q\bar{q}}.$$

The measurement uses $78\,\text{fb}^{-1}$ data sample collected with the Belle detector at the $\Upsilon(4S)$ resonance, which corresponds to 84.966 M $B\bar{B}$, and $8.3\,\text{fb}^{-1}$ off-resonance data, which was taken $\sim 60\,\text{MeV}$ below the $\Upsilon(4S)$ resonance. To simulate the $B^+ \to \rho^+\rho^0$ signal, a large Monte Carlo (MC) sample was generated by the EvtGen generator.

3.3 Kinematics of B Decays

Candidate B decays are identified using two independent variables: the energy constraint ΔE, and the beam-constrained mass M_{bc}.

Since the B mesons are produced via $e^+e^- \to \Upsilon(4S) \to B\bar{B}$, where the $\Upsilon(4S)$ is at rest in the cms, the energy of either of the two B mesons is given by the beam energy, E_{beam}. We define $\Delta E \equiv E_1 + E_2 - E_{beam}$, where E_1 and E_2 are the energies of the daughters of the B meson candidate. The ΔE distribution for signal peaks at $\Delta E = 0$, while the background distribution falls linearly in ΔE over the region of interest. The resolution of ΔE is mode dependent and helicity angle dependent (see 4.1) because of the difference in energy resolution between neutral and charged pions. For modes including neutral pions in the final state, the ΔE resolution tends to be asymmetric because of energy loss out of the back of the CsI crystals.

The energy constraint ΔE helps to distinguish between modes of the same topology. When a real K is reconstructed as a π, ΔE will peak below zero by an amount of ~ 40 MeV. Furthermore, if one or more low energy particles are missed in the B reconstruction, ΔE will peak at the lower ΔE region, while if additional particles are included in the B reconstruction, ΔE will peak at the higher ΔE region.

Figure 3.1 shows the ΔE distributions for signal $B^+ \to \rho^+\rho^0$ (solid), $B^+ \to \rho^+ K^{*0}$ (dashed) with an incorrect mass hypothesis for the kaon, and continuum background (dotted). The presence of a π^0 in both $B^+ \to \rho^+\rho^0$ and $B^+ \to \rho^+K^{*0}$ leads to the asymmetric ΔE distributions.

Since the energy of a B meson is equal to the beam energy, we use E_{beam} instead of the reconstructed energy of the B candidate to calculate the beam-constrained B mass, $M_{bc} \equiv \sqrt{(E_{beam})^2 - (p_B)^2}$. The beam constraint improves the mass resolution by about an order of magnitude, since $|p_B|$ is only 0.3 GeV/c and the beam energy is known to much higher precision than the measured energy of the B decay products. The constrained-mass resolutions range from 2.7 to 3.0 MeV, where the larger resolution corresponds to decay modes with high momentum π^0 mesons.

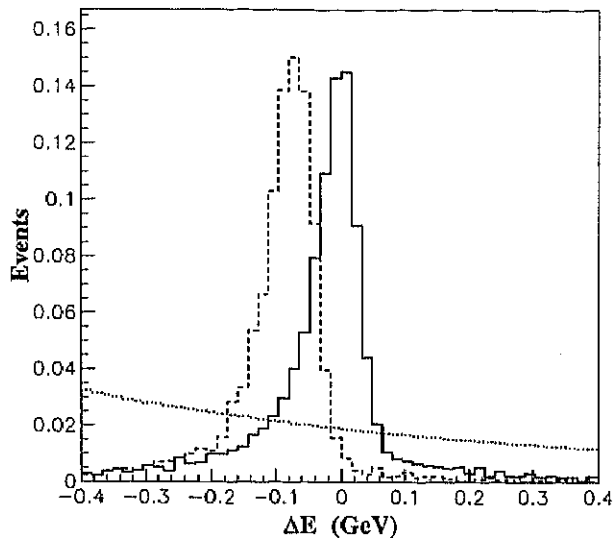

Figure 3.1: The ΔE distributions for signal $B^+ \to \rho^+\rho^0$ (solid), $B^+ \to \rho^+K^{*0}$ (dashed), where the kaon is calculated with a pion mass assumption, and continuum (dotted line).

3.4 $B^+ \to \rho^+\rho^0$ Features

The mode $B^+ \to \rho^+\rho^0$ has a final state with three charged and one neutral pion. The presence of a neutral pion results in a poor measurement resolution and low efficiency; the wide ρ mass ($\Gamma = 150.2\,\mathrm{MeV/c^2}$) leads to a high background level.

As will be discussed in chapter 4, the final state has both possibility of the longitudinal polarization state (H_{00}) and the transverse polarization state (H_{11}). For the two helicity states, the $\rho \to \pi\pi$ daughters have rather different momentum distributions. For the H_{00} state, the two pions have an asymmetric momentum distribution where one pion has low momentum (in the range $0 \sim 1.3\,\mathrm{GeV/c}$) while the other has high momentum ($1.3 \sim 2.8\,\mathrm{GeV/c}$); for the H_{11} state, the two pions tend to have the same momentum. Figures 3.2 and 3.3 show the pion momentum distributions for the H_{00} helicity state and the H_{11} helicity state from signal-MC. Because of its higher probability of having low and high energy final-state pions, the H_{00} state has a lower reconstruction efficiency, poorer ΔE resolution, and higher backgrounds. The ΔE resolution for the H_{00} state is, on average, about 1.15 times worse that for the H_{11} state.

3.5 Kinematic B Reconstruction

We select events by combining three charged and one neutral pion. We require that each charged track has a transverse momentum $p_t > 0.1\,\mathrm{GeV/c}$ in the center of mass (cms)

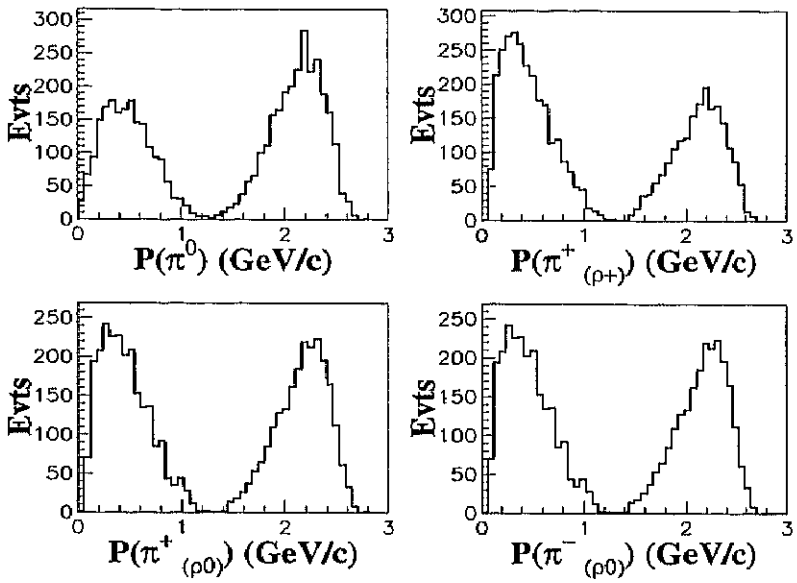

Figure 3.2: The cms momentum distributions of the final-state pions for the H_{00} state.

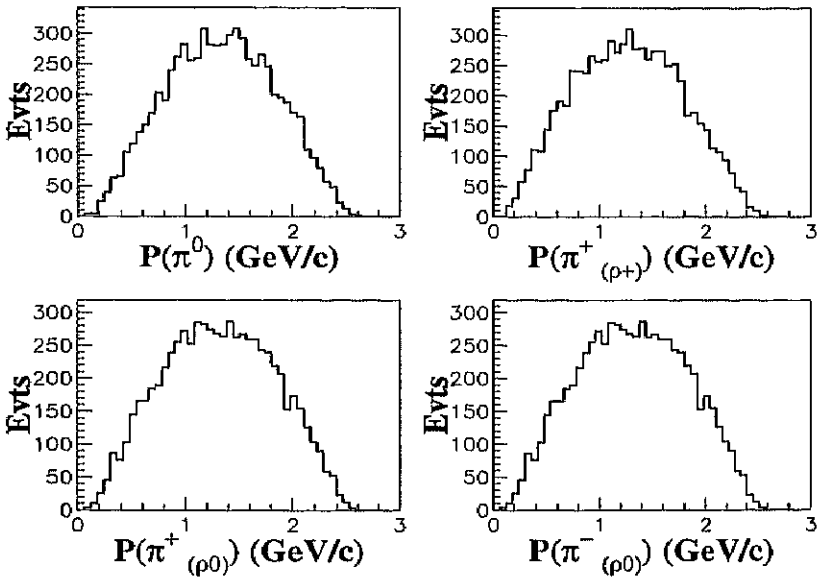

Figure 3.3: The cms momentum distributions of the final-state pions for the H_{11} state.

frame, and originates from within $dr < 0.1\,\mathrm{cm}$ in the radial direction and $|dz| < 5\,\mathrm{cm}$ in the electron direction of the run-by-run-determined interaction point. Furthermore, we fit the three charged tracks on the interaction point, and require the fitting quality ($\chi^2/ndf < 10$). Figure 3.4 shows the fitting quality for both signal MC and data. We also require that the three charged tracks are positively identified as pions ($pid(K\pi) < 0.4$) and are not consistent with being an electron ($eid < 0.9$).

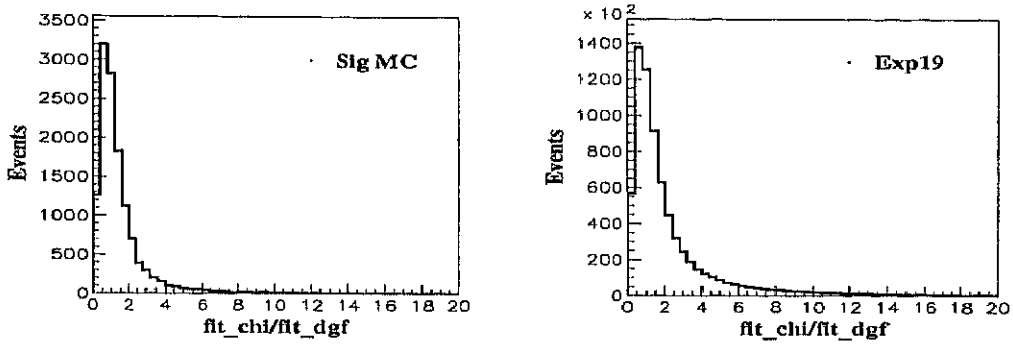

Figure 3.4: The χ^2/ndf distributions for signal MC (left) and data (right).

Candidate π^0 mesons are reconstructed from pairs of photons that have an invariant mass in the range $0.118\,\mathrm{GeV/c^2} < M(\gamma\gamma) < 0.150\,\mathrm{GeV/c^2}$. In order to reduce combinatorial backgrounds, photons in the ECL barrel region are required to have energies greater than 50 MeV; for photons in the endcap ECL this requirement is increased to 100 MeV. In addition, we only accept π^0 candidates with a cms momentum $p > 0.5\,\mathrm{GeV/c}$. Figure 3.5 shows low momentum π^0's have a large background. The π^0 candidates are kinematically constrained to the nominal π^0 mass value.

Candidate ρ mesons are reconstructed via their $\rho^0 \to \pi^+\pi^-$ and $\rho^+ \to \pi^+\pi^0$ decays. For both the charged and neutral modes, the pion pairs are required to satisfy $0.65\,\mathrm{GeV/c^2} < M(\pi\pi) < 0.89\,\mathrm{GeV/c^2}$.

Candidate $B^+ \to \rho^+\rho^0$ decays are identified using the beam-constrained mass M_{bc} and the energy difference ΔE as described. Because of the presence of a π^0 in the final state, the ΔE distribution has a tail on the lower side caused by energy leakage out of the back of the CsI crystals, and the ΔE resolution varies depending on the π^0 momentum. We use events in the region $|\Delta E| < 0.4\,\mathrm{GeV}$, $M_{bc} > 5.2\,\mathrm{GeV/c^2}$ with a signal region defined as $-0.10\,\mathrm{GeV} < \Delta E < 0.06\,\mathrm{GeV}$ and $5.272\,\mathrm{GeV/c^2} < M_{bc} < 5.290\,\mathrm{GeV/c^2}$. Figure 3.6 shows the ΔE and M_{bc} distributions for signal-MC.

As mentioned, the π^0 candidates are constrained to the nominal π^0 mass value, where an interaction point (0, 0, 0) (default) is assumed. If the mass constraint fit is performed with a more precise IP, we can, in principle, improve the ΔE resolution. This idea is

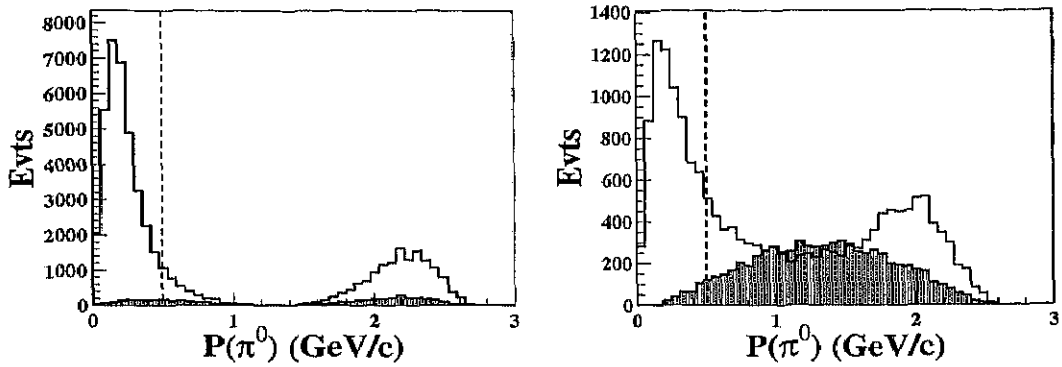

Figure 3.5: The number of events versus the π^0 momentum for the H_{00} (left) and H_{11} (right) signal MC. The hatched plots show the signal events; the open plots show the combinatorial background. A cms π^0 momentum $p > 0.5\,\mathrm{GeV/c}$ (dashed line) requirement is applied in the analysis.

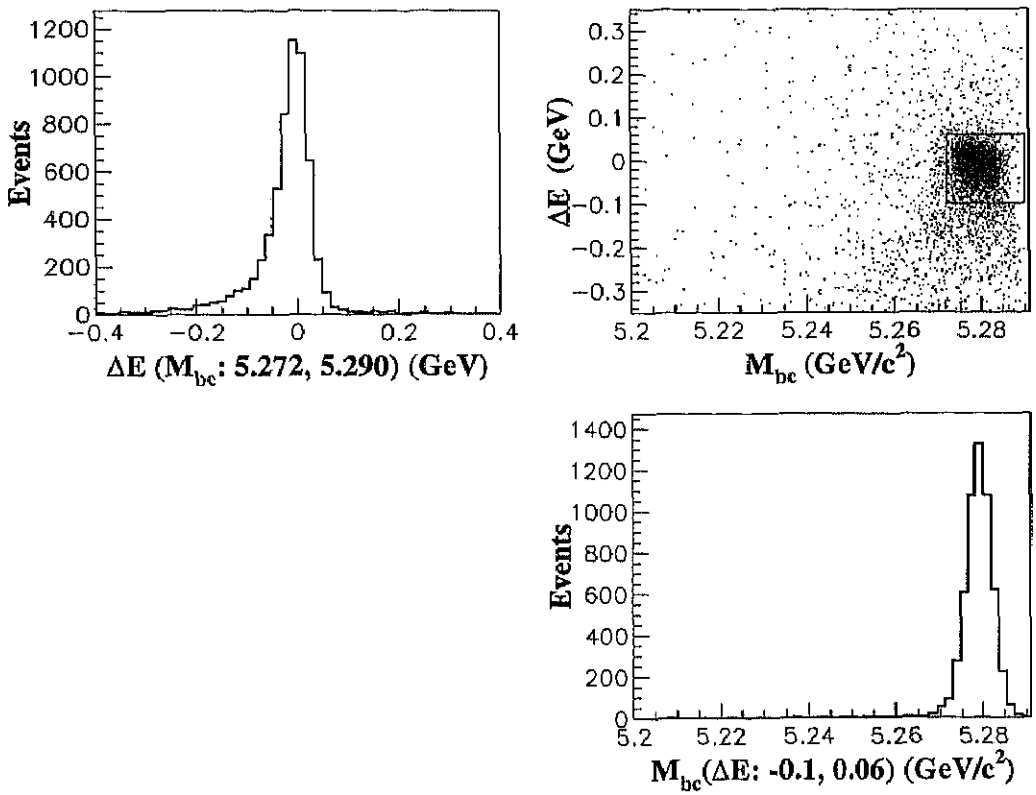

Figure 3.6: For signal-MC events,the top left plot is the ΔE distribution in $5.272\,\mathrm{GeV/c^2} < M_{bc} < 5.290\,\mathrm{GeV/c^2}$ signal region; the top right plot shows ΔE versus M_{bc}, where the box represents the signal region; the bottom plot shows the M_{bc} distribution in the $-0.10\,\mathrm{GeV} < \Delta E < 0.06\,\mathrm{GeV}$ signal region.

checked with MC as follows: for each candidate event, the IP is determined by fitting the three charged pions, π^0 candidates are then re-fitted on the determined IP. Figure 3.7 shows the resolution of ΔE obtained from the re-fitted π^0's (left), compared with that before the re-fit (right). We see no improvement in ΔE resolution. This could be because the errors of ECL position measurements are larger than the IP shift in the z direction. A default IP is used in π^0's mass constraint fit.

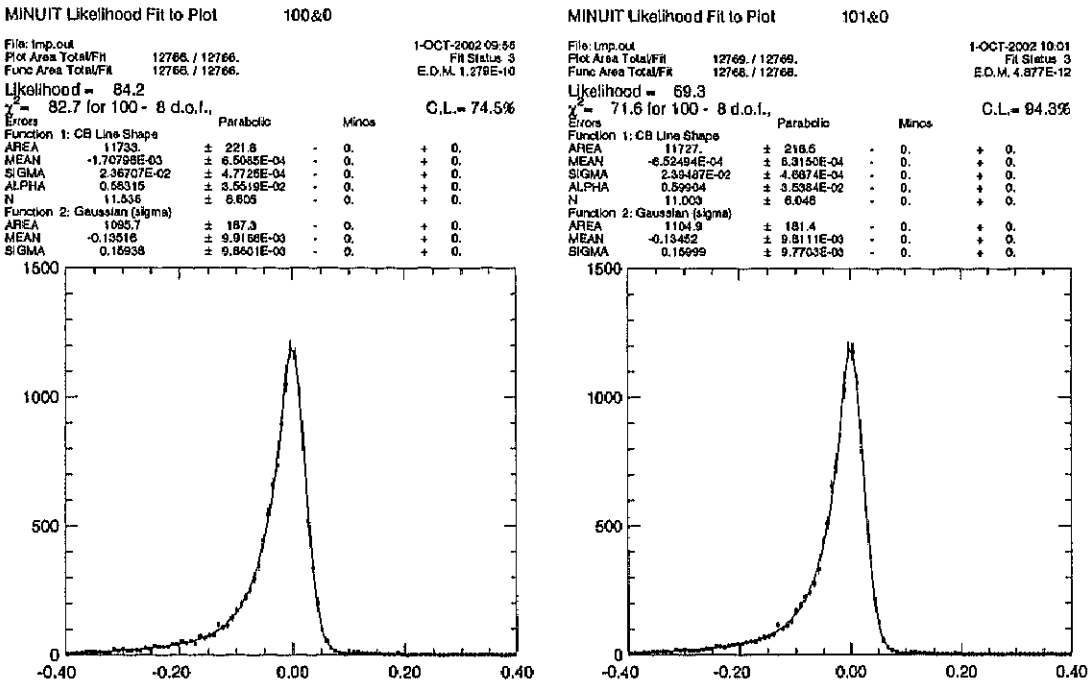

Figure 3.7: The resolution of ΔE reconstructed from the re-fitted π^0 (left), compared to that of before (right)

3.6 Continuum Suppression

As described, in the HadronB events, the dominant background is $q\bar{q}$ continuum,

$$e^+e^- \to q\bar{q} \to \text{hadrons},$$

which can produce the same final hadronic states as the signal. In general, the continuum productions have high momenta. The final cross section of the $q\bar{q}$ continuum productions is about three times that of $\Upsilon(4S)$. For a decay mode with a branching fraction of 10^{-5}, the continuum background is 3×10^5 higher than the signal. For the $B \to \rho\rho$ analysis, the continuum suppression is an important aspect.

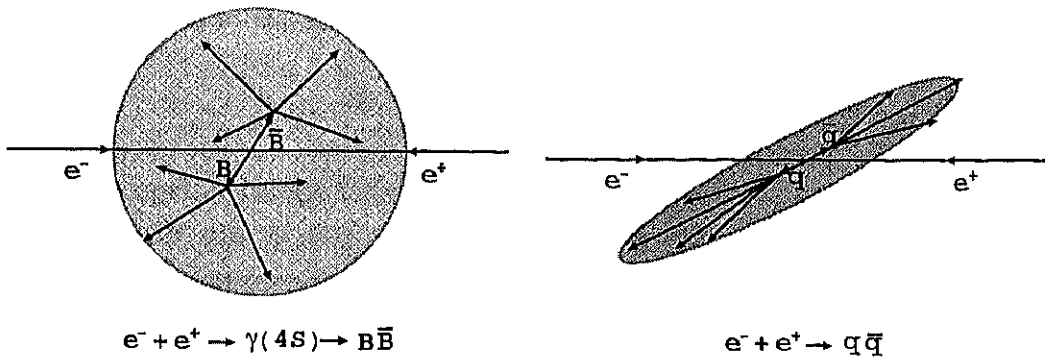

Figure 3.8: The topology for the $B\bar{B}$ events (right) and the continuum events (left).

Since in the $\Upsilon(4S)$ rest frame, the two B mesons are produced essentially at rest, and the two B decay axes are uncorrelated. However, continuum quarks are not at rest, the two quarks are back to back and hadronize along a single axis. This leads to spherical $B\bar{B}$ events and collimated jet-like continuum events, as shown in Fig. 3.8, which is exploited through event shape variables to reduce these backgrounds.

3.6.1 Topology Variables

Several topology variables are used in this analysis.

The $\cos\theta_{thr}$, where the θ_{thr} is the angle between the thrust axis of the candidate tracks and that of the remaining tracks in the event. Figure 3.9 shows the $\cos\theta_{thr}$ distributions for signal-MC (solid line) and continuum events (dashed line).

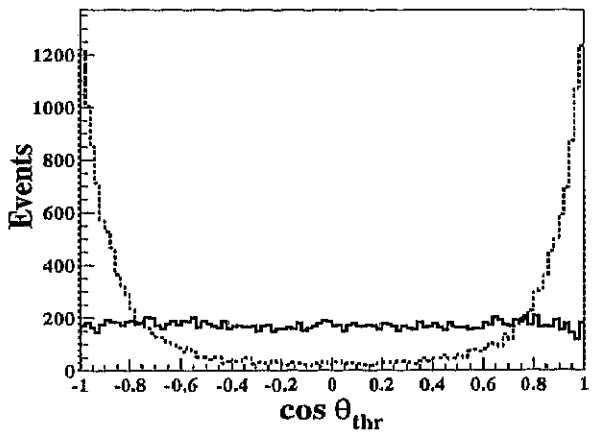

Figure 3.9: The $\cos\theta_{thr}$ distributions for signal-MC (solid) and continuum events (dashed).

Another variable usually used to quantify event shape is the normalized second Fox-

Wolfram moment, $R_2 = H_2/H_0$. The Fox-Wolfram moments are [39]

$$H_l = \sum_{i,j} |p_i||p_j| P_l(\cos\theta_{ij}),$$

where θ_{ij} is the opening angle between particles i and j, $P_l(x)$ is the lth order Legendre polynomial, and the sum is over all particles in the event.

We improve the suppression power of the Fox-Wolfram moments by taking into account which tracks come from the reconstructed B candidate (signal tracks) or the remaining tracks (other tracks) of the events. The sum can then be split into three terms

$$H_l = H_l^{ss} + H_l^{so} + H_l^{oo},$$

where H^{ss} is a double sum over signal tracks, H^{oo} is a double sum over the other tracks, and H^{so} has one index summing over signal tracks and the other over the remaining tracks. Since H^{ss} is highly correlated with the kinematic B reconstruction variables and is thus removed. For odd l, H^{so} are found to be correlative with the beam constrained mass [40] and are also removed. Information on the event topology from the first four moments is also useful. Thus, the moments H_2^{so}, H_4^{so}, H_1^{oo}, H_2^{oo}, H_3^{oo} and H_4^{oo} are used.

The modified moments are combined into a Fisher discriminant ($\mathcal{F}$). The coefficients of the Fisher discriminant are determined by optimizing the separation between the signal and the continuum MC events.

$$\mathcal{F} = \sum_{l=1}^{4} (\alpha_l H_l^{so} + \beta_l H_l^{oo}),$$

where α_l and β_l are the $\mathcal{F}$ coefficients. Figure 3.10 (left) shows the $\mathcal{F}$ distributions for the signal-MC events and the M_{bc} sideband (defined as $M_{bc} < 5.26\,\mathrm{GeV/c^2}$).

3.6.2 B Flight Direction

In addition to the event topology, there are other variables which are also somewhat useful to discriminate $B\bar{B}$ and $q\bar{q}$ events. One of these is the $\cos\theta_B$, where θ_B is the B flight direction in the cms frame with respect to the z-axis.

The $\cos\theta_B$ is distributed as $\sin^2\theta_B$ for true B events and is uniform for continuum events. Figure 3.10 (right) shows the $\cos\theta_B$ distributions for signal-MC and M_{bc} sideband events.

3.6.3 Continuum Background Suppression

In this analysis, the continuum background is suppressed by the requirement of $|\cos\theta_{thr}| < 0.8$. This requirement has an efficiency of 79% for signal-MC events, and 18% for contin-

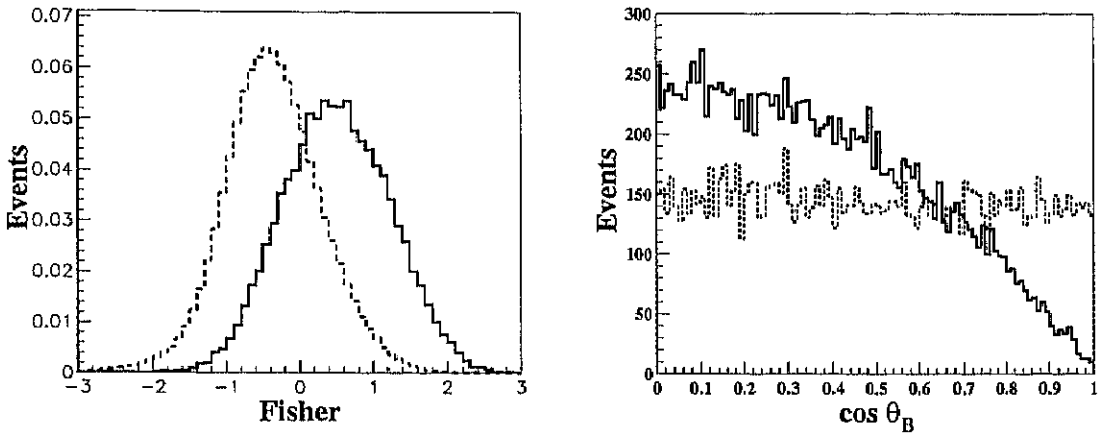

Figure 3.10: The left plot shows the $\mathcal{F}$ distributions for signal-MC (solid) and M_{bc} sideband events (dashed); the right plot shows the $\cos\theta_B$ distributions.

uum MC events.

We achieve additional suppression by means of a likelihood ratio derived from two variables. One is the Fisher discriminant $\mathcal{F}$ formed from six modified Fox-Wolfram moments, the other variable is the B flight direction $\cos\theta_B$. The $\mathcal{F}$ and $\cos\theta_B$ shapes for signal are obtained from signal-MC; for continuum, they are determined from M_{bc} sideband ($M_{bc} < 5.26\,\mathrm{GeV/c^2}$) with $-0.3\,\mathrm{GeV} < \Delta E < 0.3\,\mathrm{GeV}$. Normalized probability density functions (PDF) of $\mathcal{F}$ and $\cos\theta_B$ are multiplied to form the likelihood functions for the signal ($\mathcal{L}_{sig}$) and continuum ($\mathcal{L}_{cont}$) processes. Figure 3.11 shows the $\mathcal{LR}$ distributions for signal-MC and M_{bc} sideband. A requirement on the likelihood ratio ($\mathcal{LR}$) of $\mathcal{L}_{sig}/(\mathcal{L}_{sig} + \mathcal{L}_{cont}) > 0.85$, which is established by maximizing the figure of merit $S/\sqrt{(S+B)}$ where S denotes signal and B represents background, rejects an additional 98% of the continuum events with a 65% loss in signal. Figure 3.12 shows the ΔE and M_{bc} distributions for continuum MC after the application of all cuts, no signal-like peak is found.

3.7 $B\bar{B}$ Background

Background contributions from $b \to c$ processes are investigated with two large MC samples of generic B decays. These samples contain 44×10^6 $B^0\bar{B}^0$ and 44×10^6 B^+B^- events. After the application of all cuts, no signal-like peak is found in the ΔE and M_{bc} distributions, as shown in Fig. 3.13. The contributions of $B\bar{B}$ backgrounds are taken into account when fitting the ΔE and M_{bc} distributions.

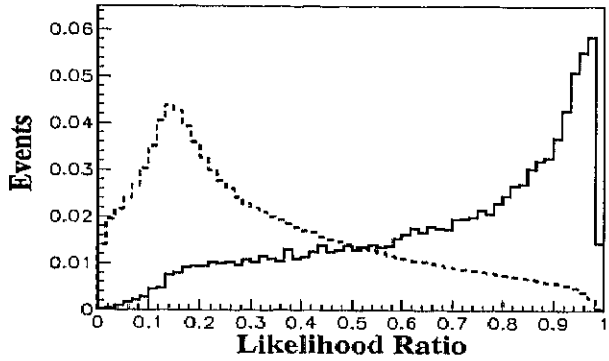

Figure 3.11: The $\mathcal{LR}$ distributions for signal-MC (solid) and M_{bc} sideband (dashed).

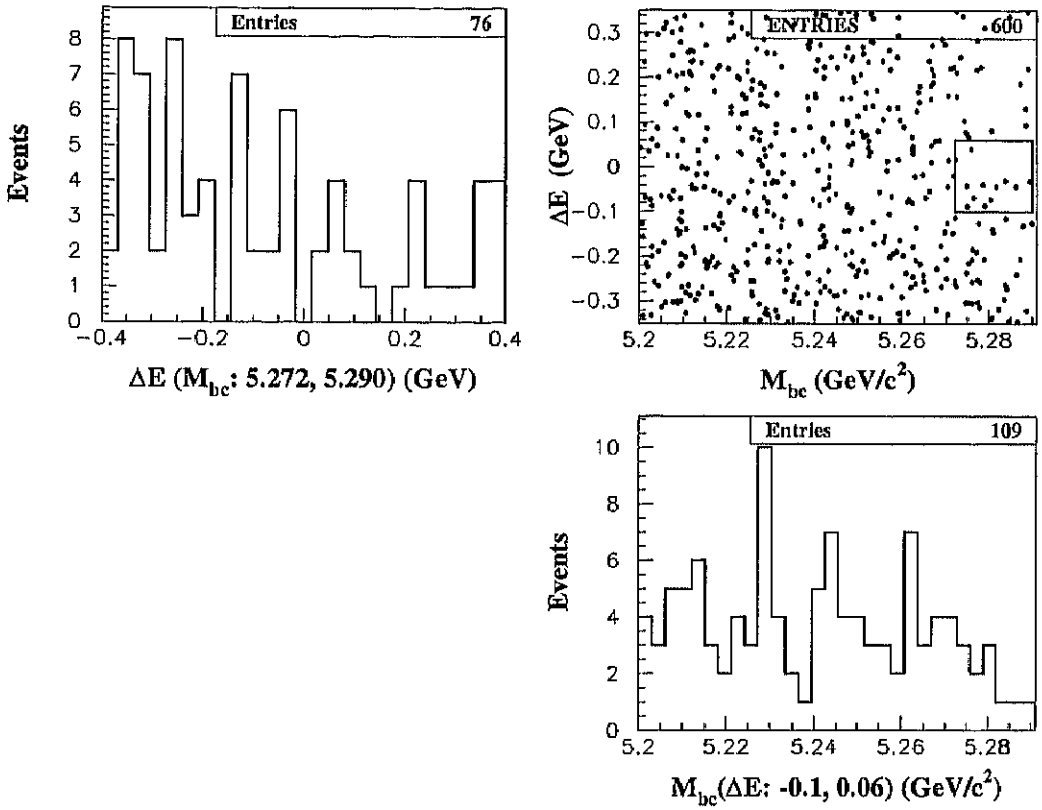

Figure 3.12: For 63 M generic continuum MC, top left plot shows ΔE distribution in the M_{bc} signal region; top right plot shows the distribution of ΔE versus M_{bc}; and bottom plot is the M_{bc} distribution in the ΔE signal region.

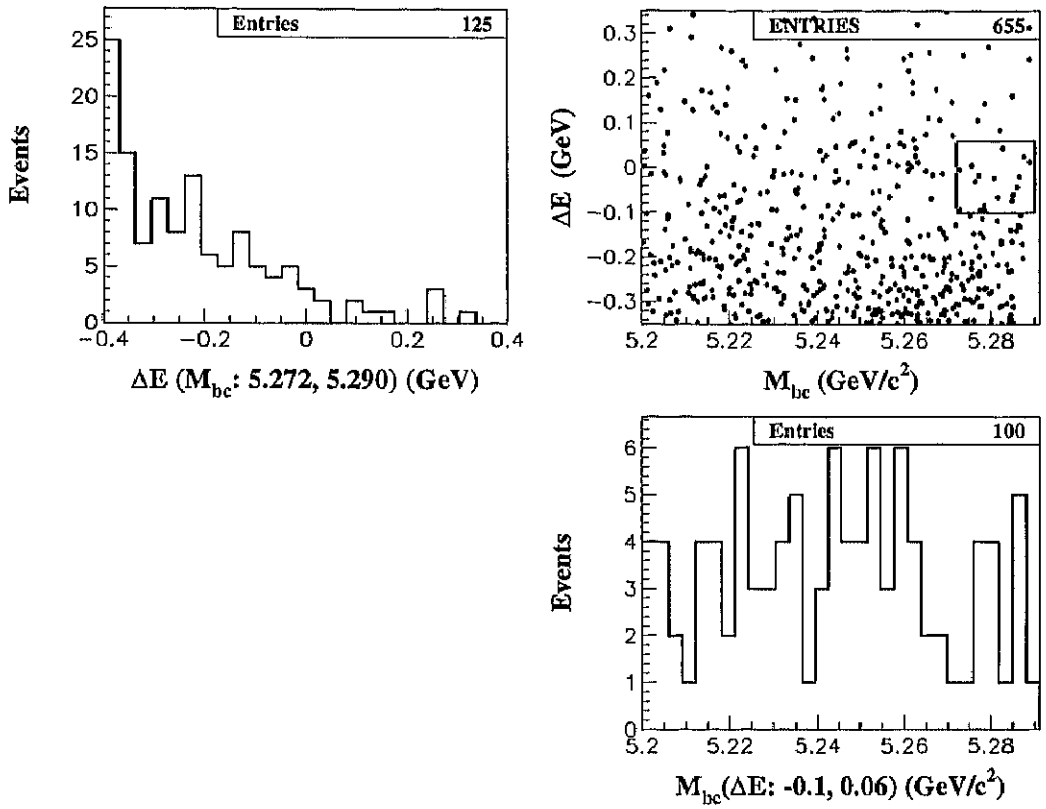

Figure 3.13: For 88 M generic $B\bar{B}$ MC, top left plot shows ΔE distribution in the M_{bc} signal region; top right plot shows the distribution of ΔE versus M_{bc}; and bottom plot is the M_{bc} distribution in the ΔE signal region.

3.8 Rare B Decay Backgrounds

There are also other rare B decay processes that can contaminate the ΔE and M_{bc} distributions; e.g. $B^+ \to \eta'\rho^+$, $B^+ \to K^*\rho$, and three-body decays of the type $B \to \rho\pi$.

However, since in each of these modes there is either a missing photon or different numbers of pions or an incorrect mass hypothesis for a kaon, these backgrounds are displaced from the signal in ΔE. Figures 3.14 to 3.16 show the ΔE and M_{bc} distributions for the decays of $B^+ \to \eta'\rho^+$, $B^+ \to K^*\rho$ and $B \to \rho\pi$ separately.

Moreover, these modes have small branching fractions [41, 42] and low reconstruction efficiencies; for the decays $B^+ \to \rho^+\eta'$, MC estimates of the yields are less than 1.4 events; for the decays $B^+ \to K^*\rho$, MC estimates of their yields are less than 5.5 events (2.6 $K^{*+}\rho^0$ events and 2.8 ρ^+K^{*0} events); for the decays $B \to \rho\pi$, 4 events (2.7 $\rho^\pm\pi^\mp$ events and 1.3 $\rho^0\pi^0$ events) are expected on the positive ΔE ($\sim 0.2\,\mathrm{GeV}$) side, 0 event is expected in signal region. Table 3.2 shows the upper limits of branching fraction for these modes, where the efficiencies are obtained from MC by counting the events in signal region after all selection requirements are applied. MC estimates of their total yields are less than seven events.

Mode	Branching Fraction	Effic.(%)	MC-expect.
$B^+ \to \eta'\rho^+$	$< 4.7 \times 10^{-5}$(PDG)	0.035	1.4
$B^+ \to K^{*+}\rho^0$	$< 5.4 \times 10^{-5}$(CLEO)	0.058	2.7
$B^+ \to \rho^+K^{*0}$	$< 2.3 \times 10^{-5}$	0.143	2.8
$B^0 \to \rho^\pm\pi^\mp$	$< 2.1 \times 10^{-5}$ (Belle)	0.005	< 0.1
$B^0 \to \rho^0\pi^0$	$< 2.8 \times 10^{-6}$ (Belle)	0.035	< 0.1

Table 3.2: The branching fractions and efficiencies for the major rare decay backgrounds.

This contamination is considered as a part of the systematic error. The detailed discussion is given in section 4.4.

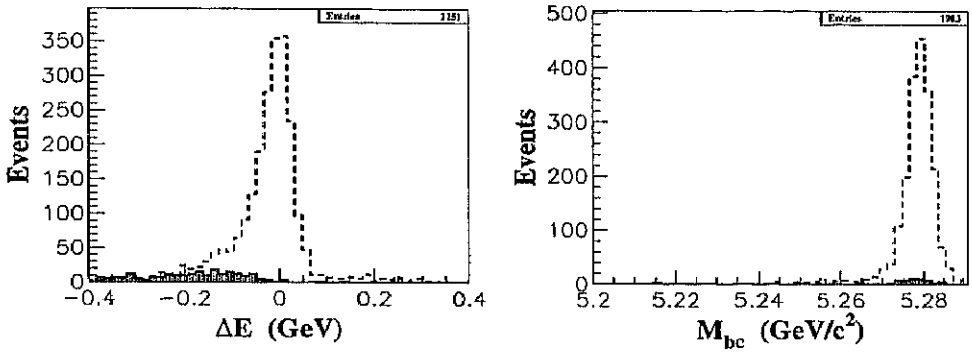

Figure 3.14: The ΔE (left) and M_{bc} (right) distributions for the decay $B^+ \to \rho^+\eta'$ from MC (hatched) assuming the branching ratio to be the upper limit listed in Table 3.2, compared with that of $B^+ \to \rho^+\rho^0$ (open).

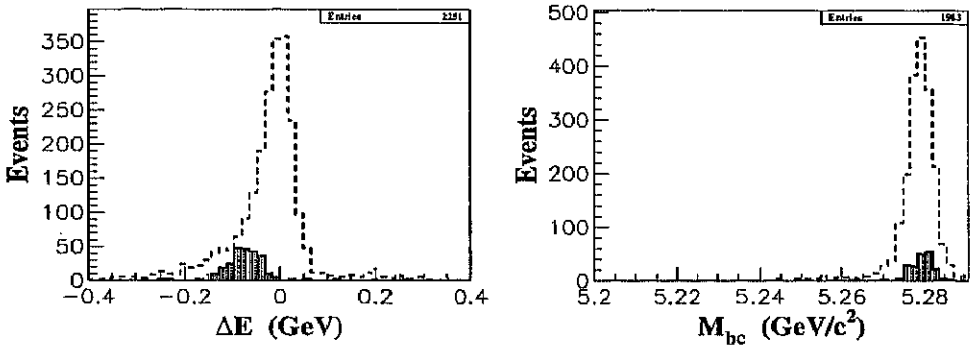

Figure 3.15: The ΔE (left) and M_{bc} (right) distributions for a sum of $B^+ \to \rho^+K^{*0}$ and $B^+ \to K^{*+}\rho^0$ from MC (hatched) assuming their branching ratios to be the upper limits listed in Table 3.2, compared to that of $B^+ \to \rho^+\rho^0$ (open).

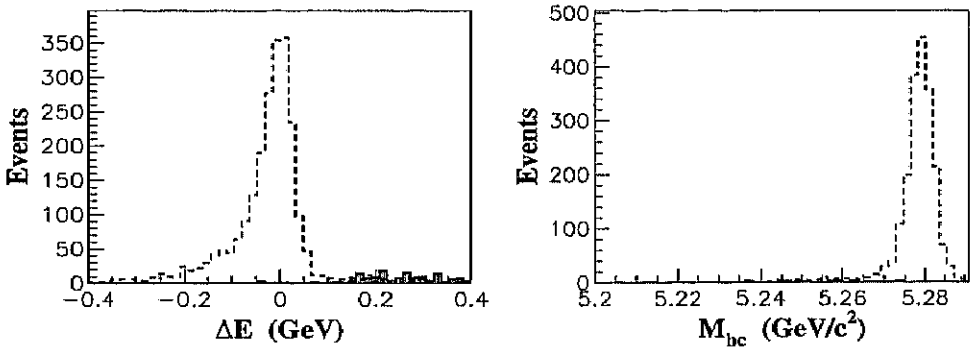

Figure 3.16: The ΔE (left) and M_{bc} (right) distributions for a sum of $B^0 \to \rho^0\pi^0$ and $B^0 \to \rho^+\pi^-$ from MC (hatched) assuming their branching ratios to be the upper limits listed in Table 3.2, compared to that of $B^+ \to \rho^+\rho^0$ (open).

3.9 Signal Extraction

The signal yields are extracted from binned maximum-likelihood fits to the ΔE and M_{bc} distributions. We use the ΔE fit result for the branching fraction calculation, and take the M_{bc} fit as a consistency check; since for rare decay backgrounds, the ΔE distribution provides additional discrimination.

3.9.1 Calibration

Before fitting data, we should understand how well the MC simulation is consistent with the data. The consistency check is performed with the decay $B^+ \to \bar{D}^0\pi^+$, $\bar{D}^0 \to K^+\pi^-\pi^0$ and its charge conjugate mode. This channel is the only one that has a π^0 in the final state, and has large statistics. The calibration results are shown in Fig. 3.17, and listed in Table 3.3. We find a $\sim$ 2.5 MeV shift in ΔE mean value between data and MC. Corrections are made when fitting the data.

	ΔE		M_{bc}	
	Mean (MeV)	σ (MeV)	Mean (GeV/c^2)	σ (MeV/c^2)
MC	-2.3 ± 0.4	22.1 ± 0.3	5.279	2.9
DATA	-4.8 ± 0.6	23.0 ± 0.6	5.279	2.7

Table 3.3: The results of the consistency check by using $B^+ \to \bar{D}^0\pi^+$ and $\bar{D}^0 \to K^+\pi^-\pi^0$ decays. The mean and σ are obtained from the fits to the ΔE and M_{bc} distributions for MC and data.

3.9.2 Results and Fits

Figure 3.18 (left) shows the ΔE projection of selected events in the 5.272 GeV/c^2 $< M_{bc} <$ 5.29 GeV/c^2 signal region. The curve shows the binned maximum-likelihood fit results. The fit is performed with three components: signal, continuum and $B\bar{B}$ contributions. The sum of a Gaussian and a Crystal Ball line shape (CB) [43] function determined from the H_{00} signal-MC calibrated with $B^+ \to \bar{D}^0\pi^+$ events is used to represent the signal. A linear function determined from off-resonance data, which was taken about 60 MeV below the $\Upsilon(4S)$ resonance, is used to represent the continuum background. The $B\bar{B}$ contribution is modeled by a smoothed histogram with a shape that is obtained from 88 M generic $B\bar{B}$ MC. In the fit, all parameters other than the normalizations are fixed.

The fit gives a signal yield of 58.7 ± 13.2 events. The statistical significance of the signal, defined as $\sqrt{-2\ln(\mathcal{L}_0/\mathcal{L}_{max})}$, where $\mathcal{L}_{max}$ is the likelihood at the nominal signal yield and $\mathcal{L}_0$ is the likelihood with the signal yield fixed to zero, is 5.3σ.

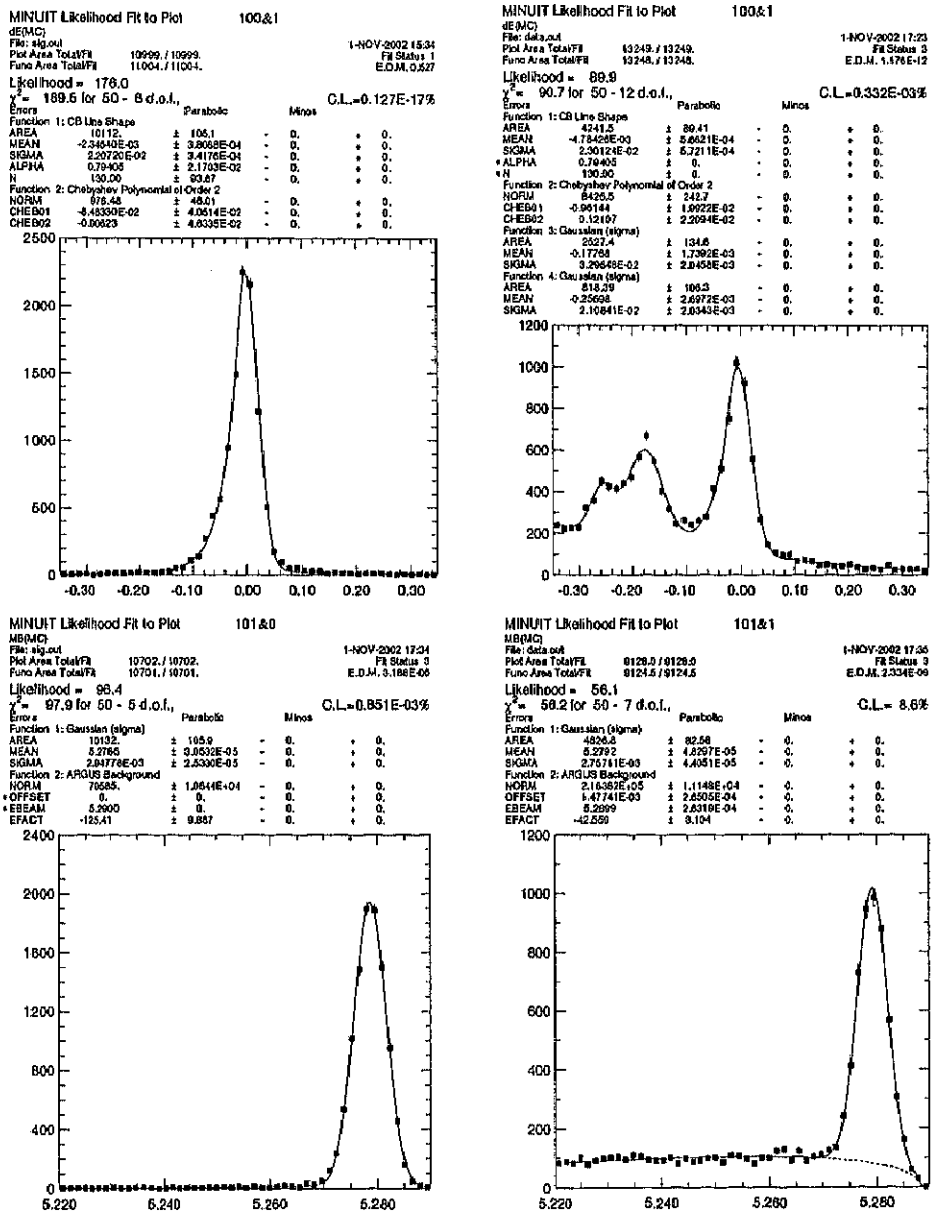

Figure 3.17: The ΔE (top) and M_{bc} (bottom) distributions for $B^+ \to \bar{D}^0\pi^+$, $\bar{D}^0 \to K^+\pi^-\pi^0$ from MC (left) and data (right). A slight shift in ΔE is found.

Figure 3.18 (right) shows the M_{bc} projection of events in the $-0.1\,\mathrm{GeV} < \Delta E < 0.06\,\mathrm{GeV}$ signal region. The curve shows the results of a binned maximum-likelihood fit that uses a signal Gaussian with a MC-determined width to represent the signal, a threshold-type (ARGUS) function [44] for the continuum background with shape parameters that are determined from the ΔE sideband (defined as $0.1\,\mathrm{GeV} < \Delta E < 0.4\,\mathrm{GeV}$), and a smoothed histogram obtained from MC to represent the $B\bar{B}$ background. The normalization of the latter component is fixed to its MC expected yield. This fit gives a signal yield of 49.1 ± 9.7, with a statistical significance of 6.5σ.

The results of the M_{bc} fit are in good agreement with the ΔE fit.

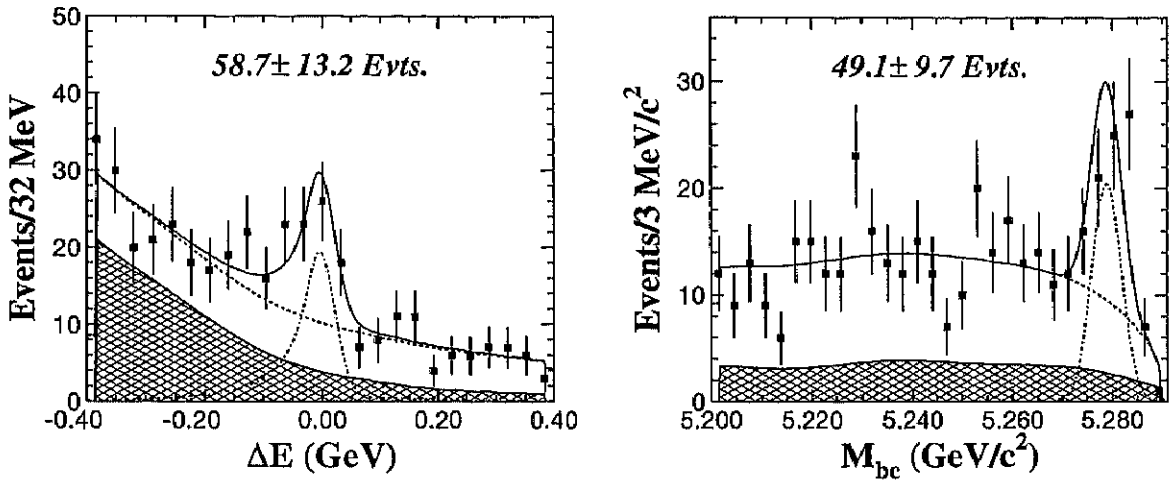

Figure 3.18: The ΔE (left) and M_{bc} (right) fit to the $B^{\pm} \to \rho^{\pm}\rho^{0}$ candidate events. The sum of the $B\bar{B}$ and continuum components is shown as a dashed line. The cross-hatched histogram represents the $B\bar{B}$ background.

3.9.3 Efficiencies

The efficiency is given by

$$\epsilon(recon.) \times \epsilon(q\bar{q}) \times \epsilon(PID),$$

where $\epsilon(recon.)$ is the reconstruction efficiency, $\epsilon(q\bar{q})$ is the $q\bar{q}$ rejection efficiency, and $\epsilon(PID)$ is the particle identification efficiency.

The reconstruction and continuum rejection efficiencies are determined from signal-MC; the error in the reconstruction efficiency is dominated by tracking, π^0 detection and signal-MC statistical error.

The particle identification efficiency is based on the results [29] of the study of the continuum D^{*+} decay chain $D^{*+} \to D^0\pi^+$, $D^0 \to K^-\pi^+$. This decay channel (and its charge conjugate decay) is chosen because the characteristic slow pion from the D^*

decays allows these events to be selected with a good signal to noise ratio without relying on particle identification. The particle identification efficiency varies slightly depending on the particle momentum, as shown in Table 3.4. An average weighted by the number

Momentum (GeV/c)	π effic.
0.50∼0.60	98.47 ± 0.16
0.60∼0.80	96.01 ± 0.14
0.80∼1.00	91.04 ± 0.20
1.00∼1.20	88.52 ± 0.22
1.20∼1.40	86.88 ± 0.25
1.40∼1.60	86.31 ± 0.29
1.60∼1.80	85.83 ± 0.31
1.80∼2.00	86.46 ± 0.30
2.00∼2.50	87.62 ± 0.18
2.50∼3.00	89.31 ± 0.18
3.00∼3.50	89.48 ± 0.24
3.50∼4.00	89.61 ± 0.37

Table 3.4: The momentum-dependent PID efficiencies with the requirement $pid(K,\pi) < 0.4$.

of events in each momentum region is taken as the pion efficiency,

$$\epsilon = \frac{n_1\epsilon_1 + n_2\epsilon_2 + ... + n_i\epsilon_i}{N}, \quad N = n_1 + n_2 + ... + n_i,$$

where n_i is the number of events in the ith bin, determined from signal-MC; ϵ_i is the particle identification efficiency for a pion with a momentum in the ith momentum region; and ϵ is the averaged pion efficiency.

The error of ϵ can be derived as

$$\begin{aligned}(\Delta\epsilon)^2 &= (\frac{\partial\epsilon}{\partial\epsilon_1}\Delta\epsilon_1)^2 + (\frac{\partial\epsilon}{\partial\epsilon_2}\Delta\epsilon_2)^2 + ... + (\frac{\partial\epsilon}{\partial\epsilon_i}\Delta\epsilon_i)^2 \\ &+ (\frac{\partial\epsilon}{\partial n_1}\Delta n_1)^2 + (\frac{\partial\epsilon}{\partial n_2}\Delta n_2)^2 + ... + (\frac{\partial\epsilon}{\partial n_i}\Delta n_i)^2 \\ &= \sum_i (\frac{n_i}{N}\Delta\epsilon_i)^2 + \sum_i (\frac{\epsilon_i}{N}\Delta n_i)^2,\end{aligned}$$

where $\Delta\epsilon_i$ is the PID efficiency error for the ith momentum region, Δn_i is the uncertainty of the number of events in the ith momentum region, given by

$$\Delta n_i = \sqrt{N\frac{n_i}{N}(1 - \frac{n_i}{N})}.$$

The PID efficiency for each pion in the final state is listed in Table 3.5. The total PID efficiency is obtained by multiplying the three charged pion PID efficiencies.

	H_{00} state	H_{11} state
$\pi^{\pm}$(from ρ^{+})	94.57 ± 1.62	89.64 ± 1.37
π^{+} (from ρ^{0})	92.89 ± 1.76	89.38 ± 1.37
π^{-} (from ρ^{0})	92.28 ± 1.80	89.35 ± 1.37
Total	81.07 ± 2.60	71.58 ± 1.90

Table 3.5: The PID efficiencies for pions in the $B^{+} \to \rho^{+}\rho^{0}$ final state and the total PID efficiency.

The total efficiencies obtained by combining the reconstruction efficiency, continuum rejection efficiency and the PID efficiency, are listed in Table 3.6.

	$\epsilon(H_{00})$	$\epsilon(H_{11})$
ΔE fit:	2.11%	3.45 %
M_{bc} fit :	1.59 %	3.07 %

Table 3.6: The M_{bc} and ΔE efficiencies for the H_{00} and H_{11} states.

3.10 Invariant Mass $M(\pi^{+}\pi^{-})$ and $M(\pi^{+}\pi^{0})$

To verify that the signal we observe is due to $B^{+} \to \rho^{+}\rho^{0}$ decay, we checked the $M(\pi^{+}\pi^{-})$ and $M(\pi^{+}\pi^{0})$ invariant mass distributions.

Figure 3.19 shows the $M(\pi^{+}\pi^{-})$ (left) and $M(\pi^{+}\pi^{0})$ (right) invariant mass spectra for events in the signal region as open histograms and for events in the M_{bc} sideband ($M_{bc} < 5.26\,\mathrm{GeV/c^2}$) as shaded histograms. In both plots the excesses of signal region events show clear peaks near the ρ mass on a relatively flat background.

The signal yields extracted from the fits to the ΔE distributions, for different $M(\pi^{+}\pi^{-})$ and $M(\pi^{+}\pi^{0})$ mass bins, are shown in Fig. 3.20 and compared with the $\pi\pi$ mass spectra from the signal-MC. Again, good agreement between the data and the $B^{+} \to \rho^{+}\rho^{0}$ MC expectations is evident.

In addition, we examined the ΔE and M_{bc} distributions for events in $M(\pi^{+}\pi^{-})$ or $M(\pi^{+}\pi^{0})$ sidebands. Figure 3.21 shows ΔE (top) and M_{bc} (bottom) for nine regions of $\pi\pi$ invariant masses: $M(\pi\pi) < 0.65\,\mathrm{GeV/c^2}$, $0.65\,\mathrm{GeV/c^2} < M(\pi\pi) < 0.89\,\mathrm{GeV/c^2}$, and $M(\pi\pi) > 0.89\,\mathrm{GeV/c^2}$. Only the plots labelled (e), which correspond to both $M(\pi^{+}\pi^{-})$ and $M(\pi^{+}\pi^{0})$ being in the ρ mass signal region, show peaks for both ΔE and M_{bc}.

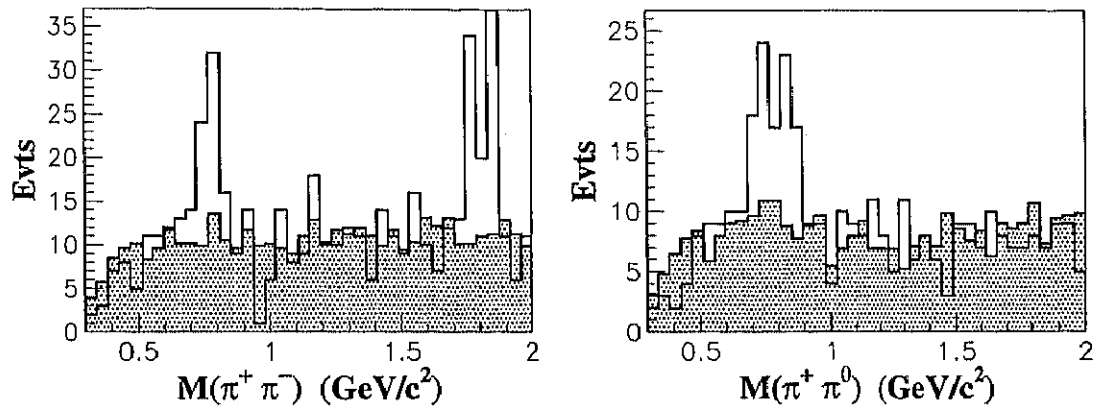

Figure 3.19: The $M(\pi^+\pi^-)$ (left) and $M(\pi^+\pi^0)$ (right) invariant mass spectra for events in signal region. The distributions from sideband events are shown as hatched histograms. The peak in higher $M(\pi^+\pi^-)$ mass is due to the contributions of $D^0 \to \pi^+\pi^-$ and $D^0 \to K^-\pi^+$ with an incorrect mass hypothesis for the kaon.

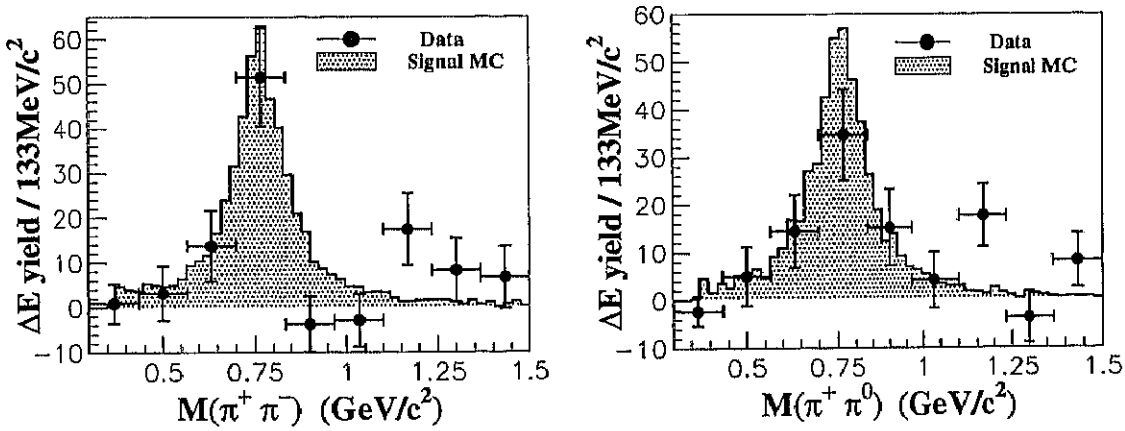

Figure 3.20: The data points are the ΔE yields in bins of $M(\pi^+\pi^-)$ (left) and $M(\pi^+\pi^0)$ (right); the distribution from signal-MC (hatched histogram) is superimposed.

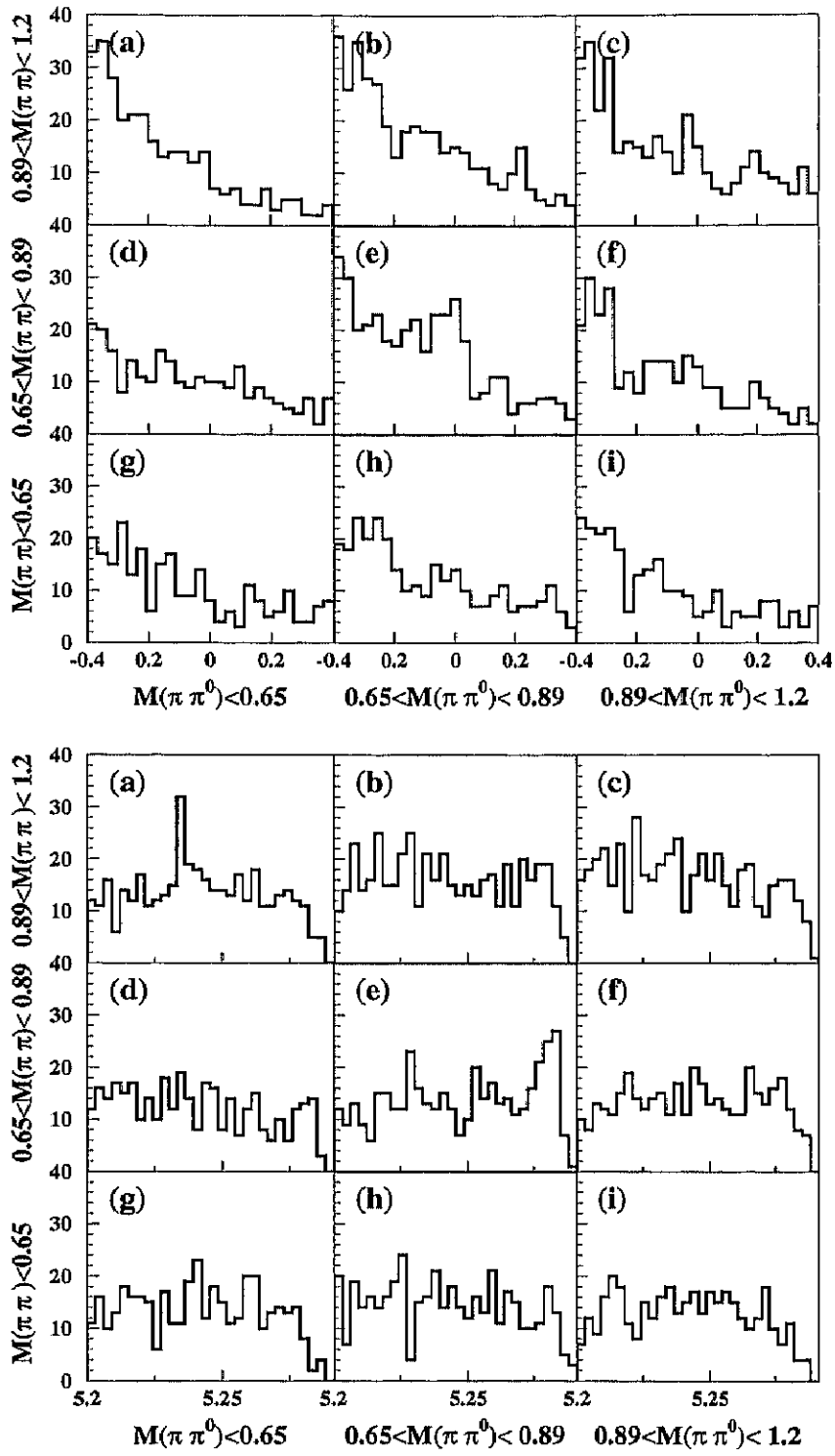

Figure 3.21: The ΔE (top) and M_{bc} (bottom) distributions for nine different $\pi^+\pi^-$ and $\pi^+\pi^0$ mass regions. The upper row plots are for $M(\pi^+\pi^-) > 0.89$ GeV/c^2 and, from left to right, $M(\pi^+\pi^0) < 0.65$ GeV/c^2, $0.65 < M(\pi^+\pi^0) < 0.89$ GeV/c^2, and $M(\pi^+\pi^0) > 0.89$ GeV/c^2. The middle and lower rows show corresponding plots for $0.65 < M(\pi^+\pi^-) < 0.89$ GeV/c^2 and $M(\pi^+\pi^-) < 0.65$ GeV/c^2, respectively.

3.11 Contributions From Non-resonant States

We examined the possible contribution from non-resonant processes using three MC-generated samples: $B^+ \to \pi^+\pi^-\pi^+\pi^0$ decays , $B^+ \to \rho^+\pi^+\pi^-$ decays, and $B^+ \to \rho^0\pi^+\pi^0$ decays, where the final states are distributed uniformly over phase space. After the application of all selection requirements, we measure the efficiency for each mode by counting the events in signal region. The efficiency for each mode is listed in Table 3.7; the total is 15% of that for $B^+ \to \rho^+\rho^0$.

Mode	Effic. (%)	Effic. relative to $\epsilon_{\rho\rho}$
$B^+ \to \pi^+\pi^-\pi^+\pi^0$	0.03	1.7%
$B^+ \to \rho^+\pi^+\pi^-$	0.10	5.8%
$B^+ \to \rho^0\pi^+\pi^0$	0.13	7.6%

Table 3.7: The efficiencies for various non-resonant modes after all requirements are applied.

The background subtracted $M(\pi\pi)$ distributions, compared with the distributions from the non-resonant $B^+ \to \pi^+\pi^-\pi^+\pi^0$ normalized to the area of the signal, is shown in Fig 3.22. The observed mass distributions are not consistent with the non-resonant decays.

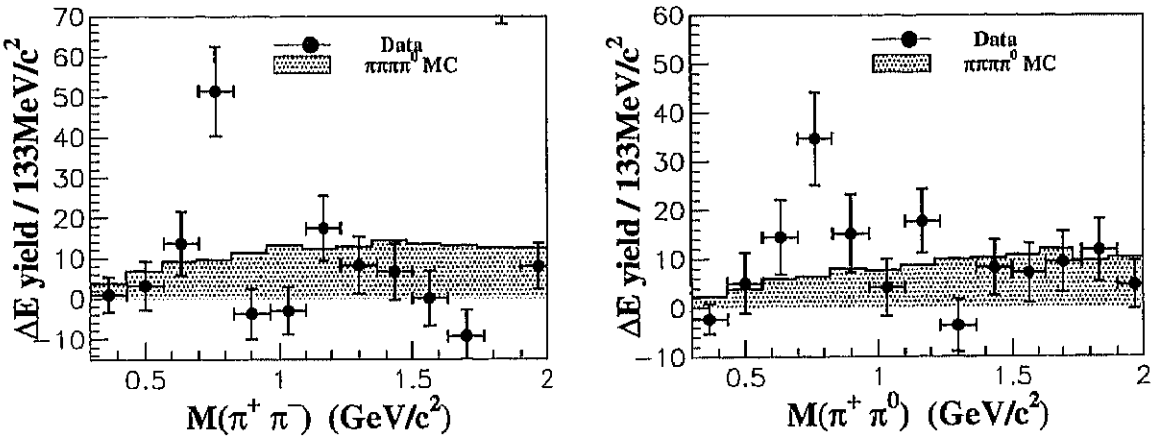

Figure 3.22: The yield from ΔE fits versus $M(\pi^+\pi^-)$ (left) and the ΔE yield versus $M(\pi^+\pi^0)$ (right), compared to the distributions from non-resonant decay $B^+ \to \pi^+\pi^-\pi^+\pi^0$ signal-MC (hatched histogram) normalized to the area of the signal.

In the present analysis, we apply relatively tight ρ mass cuts ($0.65\,\mathrm{GeV/c^2} < M(\pi\pi) < 0.89\,\mathrm{GeV/c^2}$), and ignore the possibility of such contributions.